Physics – Uspekhi **62** (6) 602 – 616 (2019) © 2019 Uspekhi Fizicheskikh Nauk, Russian Academy of Sciences

INSTRUMENTS AND METHODS OF INVESTIGATION PACS numbers: 42.25.Fx, 42.25.Kb, **61.72.–y**, 61.72.Ff, 61.72.Lk

Study of micropores in single crystals by in-line phase contrast imaging with synchrotron radiation

T S Argunova, V G Kohn

DOI: https://doi.org/10.3367/UFNe.2018.06.038371

Contents

1. **Introduction** 602
2. **Micropores in SiC single crystals and their properties** 603
3. **Theory of in-line phase-contrast imaging technique with synchrotron radiation** 606
4. **Experimental studies of micropipes in silicon carbide single crystals by the phase contrast method** 608
5. **Computer simulation of images and inverse problem solution** 612
6. **Conclusions** 614

References 615

Abstract. **Some single crystals that are of importance for engineering contain micropores of various shapes, including micropipes, empty cylinders whose section sizes vary from fractions of a micrometer to several micrometers. We describe the properties of such objects in a silicon carbide single crystal and a method of observing and exploring these objects, namely, in-line phase contrast imaging with synchrotron radiation. We also review the history of the development and current status of this method.**

Keywords: single crystals, silicon carbide, micropores, micropipes, phase contrast, synchrotron radiation

1. Introduction

Monocrystalline materials are a rarity in nature, and special conditions are, as a rule, required for their formation. However, they enjoy wide use in different realms of technology owing to their unique properties. It will suffice to recall that monocrystalline silicon (Si) with a very low lattice defect density serves as the basis of modern electronics. In new-generation electronic devices, use is made of other single crystals, both semiconductors and insulators. An example of a new industrially mastered material is silicon carbide (SiC) — a wide-band-gap semiconductor, whose merits are a high breakdown voltage (an order of magnitude higher than for silicon) and high heat conductivity, high thermal stability, chemical resistivity, and radiation resistance. Despite the fact that the quality of SiC single crystals does not yet meet the highest standards, the interest in them is due to the demand for substrates for devices of high-current fast electronics, microwave electronics, and optoelectronics [1–3].

Micropores of various natures are a problem which hinders the production of high-quality substrates. Among the requirements imposed on SiC substrates, mention should be made of a low micropore density: < 5 cm^{-2} [2]. Meeting this requirement, along with the need for structurally uniform large-area substrates, results in a high substrate cost. The pores appear during SiC single crystal growth under certain physicochemical conditions. Knowing the nature of micropore formation, it is possible to determine the growth conditions, whereby pore formation is possible to control. Micropore research is therefore a topical scientific and practical task.

SiC crystals grown on seeds by sublimation contain micropores of a tubular shape, which are termed micropipes (MPs). The nature of these defects was explained proceeding from the Frank theory: hollow tubes of radius r may be formed at screw superdislocations with large Burgers vectors b, eliminating the formation of high-stress domains about dislocation lines, with $r \sim b^2$ [4, 5]. The main contribution to the development of low-density MP monocrystal production technology was made by those methods which permitted researchers not only to observe MPs but also to determine their quantitative characteristics. The radius r may be determined by scanning electron microscopy (SEM) [6] or by atomic force microscopy (AFM) [7], and the Burgers vector by X-ray diffraction topography [6], AFM [8], transmission electron microscopy (TEM) [9], or polarization optical microscopy [10].

Determining the characteristics of micropipes resulted in the development of different models of their formation [7, 9, 11–13], which favored progress in high-quality crystal production. The lowering of micropipe density was achieved by suppressing their nucleation centers: second phase inclusions and defect boundaries as well as structural inhomogeneities at the initial growth stage. During the first decade of the

T S Argunova [(1)], **V G Kohn** [(2)]
[(1)] Ioffe Institute,
ul. Politekhnicheskaya 26, 194021 St. Petersburg, Russian Federation
[(2)] National Research Center "Kurchatov Institute",
pl. Akademika Kurchatova 1, 123182 Moscow, Russian Federation
E-mail: [(1)] argunova2002@mail.ru, [(2)] kohnvict@yandex.ru

Received 16 April 2018, revised 15 June 2018
Uspekhi Fizicheskikh Nauk **189** (6) 643 – 658 (2019)
DOI: https://doi.org/10.3367/UFNr.2018.06.038371
Translated by E N Ragozin

21st century, the micropipe density in industrial monocrystals $\geqslant 150$ mm in diameter was lowered from 1–5 cm^{-2} [14] to < 0.1 cm^{-2} [15]. Today, SiC monocrystals from the largest world manufacturers have reached the structural perfection required for making high-power devices.

In this review, we outline a relatively new method which permits one to obtain information about the size, shape, and density of micropipes without damaging the sample. This method is not a routine diagnostic tool and shows great promise for the investigation of nearly perfect monocrystals. The case in point is in-line phase-contrast imaging with synchrotron radiation (SR). The development of the new method is topical, because the capabilities of each of the above methods have various limitations.

For instance, SEM and AFM surface-sensitive methods reveal pits and growth spirals at the sites where MPs reach the growth surface. However, the pit shape does not reflect the shape of an MP throughout its path through the crystal. The relatively low resolution of optical microscopy does not make it possible to see the morphological details of small MPs. The resolution of the TEM method, by contrast, is so high that MPs may not occur in the field of view of a microscope in the investigation of samples with a low MP density. X-ray topography does not show the MP morphology and reveals only the defects associated with lattice distortions.

A relatively complete picture with micropipe images may be obtained by X-ray in-line phase-contrast imaging. The microscopic variation of crystal thickness along the ray paths caused by the appearance of a micropore gives rise to a noticeable phase shift of the coherent X-ray radiation transmitted through the sample, which results in a bending of the surface of the constant phase. At some distance from the sample, the phase-front curvature leads to a nonuniform radiation intensity distribution, which may be measured with a detector.

It is evident that spatial intensity variation of this type does not entail an integral intensity variation, since both sources and absorbers of radiation are absent in empty space. Although the effect of writing the radiation wavefield phase in its transformation to intensity has long been known and has been widely used in holography (for instance, in the Gabor scheme [16]), in X-ray optics these methods were not used for a long time due to the low coherence of X-ray sources and the low resolution of X-ray detectors, because X-ray holographic speckles are very small in size.

The situation changed radically in the mid-1990s. As many as four methods for recording phase-contrast images were proposed and came under development: the method based on the Bonse–Hart interferometer, the method involving the recording of angular deflections with crystal diffraction, the method employing periodic gratings, and, lastly, in-line phase-contrast imaging, which is similar to Gabor holography. To date, several reviews have been published which describe the indicated methods and give references (see, for instance, Refs [17–21]).

The in-line phase-contrast imaging technique is distinguished for the simplicity of experimental arrangement. Apart from the source, sample, and detector, nothing else is required. Its special feature is that the contrast can be observed only under a high spatial and temporal coherence. This is provided by modern third-generation synchrotron radiation sources [22, 23], which have a relatively small angular size and, as a consequence, a sufficiently high spatial coherence, but nevertheless rank below optical lasers in coherence. As for temporal coherence, it is provided by monochromators based on crystal diffraction.

Furthermore, the in-line method calls for modern equipment, for instance, detectors with a high spatial resolution capable of detecting a small number of photons, as well as precision goniometers. On the other hand, unlike other setups for X-ray phase-contrast formation, the in-line method does not require optical elements like gratings, focusing elements, or crystals in the position of Bragg reflection.

This review is arranged as follows. In Section 2 we describe the main types of micropores in SiC monocrystals and their properties. The third section outlines the history of the development of in-line phase-contrast imaging theory and describes the methods and problems involving the solution to the inverse problem of calculating the phase variation profile from the measured intensity profile. Also covered are some results of the application of this method in tomography. Outlined in Section 4 are the results of experimental micropipe research in silicon carbide crystals under a low temporal coherence. Section 5 is concerned with the method to solve the inverse problem of obtaining micropipe section sizes from experimental images. Also described in Section 5 are the experimental data which are inexplicable in the context of the existing theory. In conclusion, we consider an example of applying the method to other objects and outline the prospects for its development.

2. Micropores in SiC single crystals and their properties

The pores which appear simultaneously with lattice formation are characteristic of the monocrystals of various compounds. Pores in the form of pipes of micro- and nanometer-sized cross sections have been discovered in silicon carbide, garnet ferrites, $YBa_2Cu_3O_7$, and gallium nitride [24–27]. A striking example of primary pore formation is the crystallization of silicon carbide: for a low supersaturation, it grows by forming spirals caused by screw dislocations [5, 28–30]. The helix pitch is equal to an integer number of the unit cell dimension of a given SiC polytype in the direction of the dislocation axis. On the synthesized crystal surface at the center of a large spiral is a void. According to the Frank theory [4], this void is formed in the most deformed domain around a dislocation with a large Burgers vector $b > 1$ nm. The radius r of this micropipe is directly proportional to the square of the Burgers vector b:

$$r = \frac{Gb^2}{8\pi^2\gamma}\,, \tag{1}$$

where γ is the specific energy of the free crystal surface and G is the shear modulus assuming isotropy.

The demand for a material of high structural perfection for electronic engineering has led to the development of methods for artificial SiC monocrystal growth. The early 1980s saw the development of the method of crystal growth on a seed by chemical vapor deposition, the sublimation method [31], which permitted the crystal size to be significantly increased. It was possible to master the industrial production of large-diameter ingots. Early in the production of commercial crystals, their tubular micropore distribution density was high: $\geqslant 10^5$ cm^{-2} [32]. Since the pores are a serious hazard for the operation of SiC-based devices [33], major efforts were mounted to form the growth conditions

that hinder their mass nucleation. The study of MPs in SiC became a topical problem, which gave rise to a wealth of publications.

The validity of Frank's formula (1) was repeatedly verified by different methods and even by several methods simultaneously. For instance, the authors of Ref. [30] investigated a 6H-SiC crystal by phase-contrast optical microscopy, optical interferometry, and X-ray topography. Relatively poor agreement was obtained between the spiral step height and the magnitude of the Burgers vector of the screw dislocation, as well as between the diameter of voids on the surface and in the crystal volume. In the view of the authors, the disagreement was caused, in particular, by the large angular divergence of the collimated beam from the X-ray tube.

The question of whether the MPs are screw dislocations with hollow cores has been under discussion in the scientific literature for several years. An affirmative answer was obtained in the mid-1990s by performing X-ray topography experiments with white SR [6]. The magnitude of the Burgers vector calculated from a series of topograms and the hole radius at the spiral center measured by the SEM technique satisfied the relation $r \sim b^2$ well for the average value of γ/G from the interval $(1.1-1.6)\times10^{-3}$. In this case, the MP diameters ranged from 0.1 μm to several micrometers, and the typical superdislocation Burgers vectors b were equal to 2–7c in magnitude, where c is the parameter of a unit cell of the SiC polytype. Further studies by the same authors with the use of an original method of simulating topographic superdislocation images resulted in new confirmations of the Frank theory and also led to the development of a model of MP nucleation on second phase inclusions [12].

Note, however, that at about the same time, MPs were described as superdislocations of a mixed type nucleated at the clusters of stacking faults [8, 9, 11]. In the framework of different models (see also Refs [7, 10, 13]), there invariably arose the question of why elementary dislocations ($b = 1c$) of the same sign are attracted to each other to form superdislocations. A general opinion was formed that the latter are produced by reactions between dislocations in the regions where they pile up: at the boundaries of misoriented domains, the inclusions of other polytypes, etc.

Figure 1 depicts images of micropipes in SiC crystals obtained by various methods. On the X-ray topogram of Fig. 1a measured in white SR, the micropipes , whose axes are perpendicular to the surface with the orientation (0001), are visible due to their dislocation nature [34]. The SEM image of similarly oriented MPs was obtained from a surface subjected to chemical etching in the solution of potassium hydroxide (KOH) up to the appearance of pits (Fig. 1b). Spiral crystal growth is demonstrated by the SEM image of its surface (Fig. 1c). In the optical micrograph of a 4H-SiC sample, the MPs have their origin near the horizontal boundaries and propagate along the growth direction $\langle 0001 \rangle$ denoted by the arrow directed upwards (Fig. 1d). The boundaries separate the layered inclusions of other polytypes, 6H and 15R in this case. Both of these polytypes have hexagonal unit cells with the same parameters a and b; however, their cell heights differ from each other [5]: $c = 15.11$ Å and $c = 37.70$ Å, respectively. For the main polytype 4H-SiC, parameter $c = 10.05$ Å.

Similar agglomerations of MPs along the polytype boundaries are a highly typical phenomenon, which takes place due to their reactions with these boundaries [35]. During crystal growth, the dislocated pipes accumulate to combine in macropores [36]. The thus nucleated pores may continue to grow by absorbing new MPs [37].

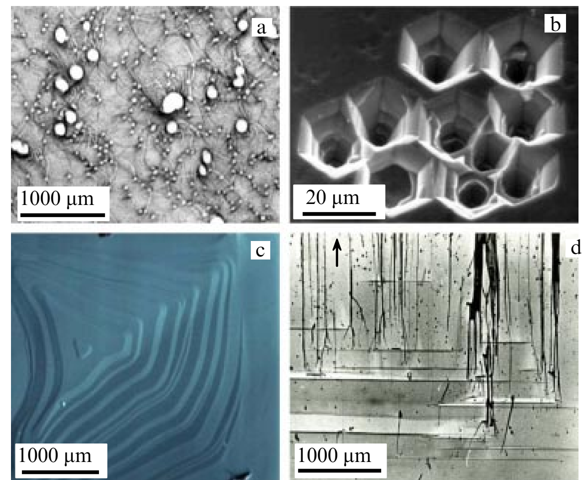

Figure 1. Micropipe images in SiC monocrystals. (a) X-ray reflection topogram of a 6H-SiC (0001) plate in white SR. The round images of screw superdislocations were obtained for the following parameters: 00024 reflection, main wavelength $\lambda = 1.25$ Å, distance to the film of 20 cm. The low-contrast lines connecting the superdislocations are basal plane dislocations [34]. (b) Micropipes on the surface of a 6H-SiC (0001) sample [42]. SEM method. (c) As-grown surface of a crystal obtained by the sublimation method. SEM method. (d) Optical micrograph of a 4H-SiC $(1\bar{1}00)$ plate [137]. The growth direction is indicated with an arrow.

Unlike pores, the pipes about screw dislocations in SiC crystals exhibit unusual properties inherent only in such objects: they interact with each other. The following MP configurations were experimentally discovered: dislocation bundles; merged MPs, when two pipes combine into one; spirals made up of two or more MPs; and semiloops terminating double spirals [38, 39]. These interactions may exert an appreciable effect on the structural perfection of the crystal by lowering or increasing the MP distribution density during its growth. To reveal the mechanisms of lowering the density of these defects, computer simulations were made of the behavior of a dislocation pipe ensemble during crystal growth [40, 41]. Reactions of merging of pipes with dislocations of opposite signs were observed, which led either to a decrease in the total Burgers vector, and consequently in the MP diameter, or to the annihilation of the dislocations and MP overgrowth. Such reactions occurring at the sites of MP accumulation may be conducive to the lowering of MP density [42, 43].

As the growth methods were improved, the number of structural defects in SiC monocrystals became lower and the ingot diameters rose up to > 150 mm [14, 15]. In 2007, American company Cree Ins., the world leader in silicon carbide production, announced an outstanding achievement: it was possible to obtain n-type SiC substrates 100 mm in diameter, which did not contain a single MP. This event was preceded by extensive research performed in laboratories in various countries.

By comparing published research results, it is possible to reveal several contradictions in the explanations of SiC micropore properties. In particular, mention should be made of a wide spread in surface energy values γ in the work of those authors who verified the validity of Frank's formula.

It may be assumed that the MP formation is largely determined by the kinetics of nucleation and interaction of defects rather than by Frank's thermodynamics. In one of the early papers, it was noted that dislocations are capable of transforming into MPs by varying growth conditions [44], temperature and pressure, in particular, which may provoke point defect migration over dislocation cores.

Furthermore, none of the methods employed to study MPs provided the opportunity to observe the morphology of these defects at the microlevel. Instruments like an optical microscope with Nomarski differential interference contrast or a scanning electron or atomic-force microscope quite well reveal growth spirals and pits on the growth surface. A transmission electron microscope records the diffraction image of a dislocation whose line passes inside a pipe. X-ray topography techniques are highly sensitive to stress fields but are not characterized by a high resolution.

Note that researchers who used the last two methods for studying MPs disagreed about the type of dislocations inside the pipes [6, 9]. They were nevertheless unanimous in their opinion that the MP has the shape of a cylinder whose radius is constant along its axis. Is this really so? Only phase-contrast images may provide the answer to this question, since they contain information both about the MP shape and about its microscopic changes. In-line imaging with SR permits morphology variations to be traced throughout the MP propagation path in the crystal. Proceeding from the thus obtained data, which are outlined below, it was possible to develop an alternative mechanism of the dislocation transformation to micropipes.

The features of micro- and macropores considered above do not exhaust the diversity of pore properties in SiC monocrystals. Some of them remain to be explained. In-line phase-contrast imaging may be highly useful in studying them, provided approaches to image simulations are developed. When the pore size does not exceed several micrometers and the pore images are measured in the far-field, i.e., far from the sample, using spectrally broad radiation, computer simulation is the only way to solve the inverse problem.

A micropipe is a quasi-linear object, in which the electron density varies rapidly across the axis and slowly along it. That is why the intensity distribution across the axis at every selected cross section may be fitted ignoring the axial dependence. This one-dimensional approach provides the possibility of obtaining information about the cross section size along and across the beam, provided that there are no abrupt shape variations along the pipe axis within the diameter of the first Fresnel zone. However, a quantitative description of the micropores of quasi-spherical, slightly prolate, faceted, or other shapes calls for invoking two-dimensional calculations.

By way of example, consider silicon carbide produced with a modified technology for which the above problems are irrelevant. In several papers (see, for instance, Ref. [45]) use was made of $(11\bar{2}0)$- and $(1\bar{1}00)$-oriented SiC seeds. The modified technology was aimed at the complete elimination of MP nucleation, which is characteristic only of the SiC growth on the basal plane (0001)-oriented seeds. Based on these investigations, Nakamura [46] developed a technology for growing crystals of high structural quality. Then, a study was carried out with the repetition of this technology, in which, however, a new feature was used for the purpose of lowering the density of dislocations growing from the seeds [47]. On the growth surface of the $(1\bar{1}00)$-oriented seed, an artificial relief was mechanically made in the form of grooves 50–80 μm wide and deep, which separated 500 × 500-μm sized areas.

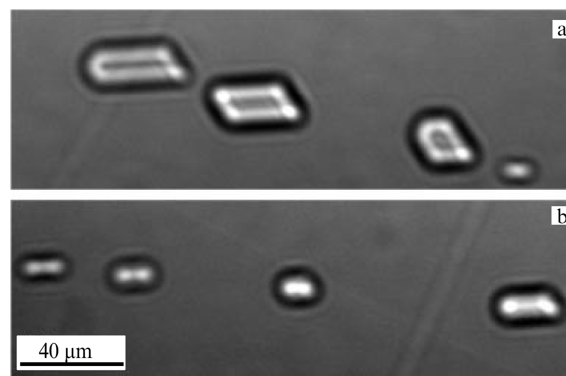

Figure 2. Far-field phase-contrast images of micropores [156]. A 6H-SiC crystal was grown in the $\langle 1\bar{1}00\rangle$ direction. The distance to the detector is equal to 40 cm. Photon energy $E = 16$ keV and $\Delta E/E = 0.02$. The transverse coherence length is equal to 21 μm. (a) Faceted pores. (b) Micropores with smoothed edges.

In the samples with a (0001)-oriented surface prepared from such an ingot, there were no MPs parallel to the $\langle 0001\rangle$ axis. Nevertheless, these crystals also had micropores. Some of them had the shape of varied diameter pipes, whose axes were oriented perpendicular to the $\langle 0001\rangle$ direction. The edges of other pores were faceted. The shape of the smallest-size pores was smoothed to ovals or capsules. Figure 2 shows small pores in an SiC sample, which appeared in the course of crystal growth in the $\langle 1\bar{1}00\rangle$ direction. They were revealed by in-line imaging with SR. Such pores may well be formed by vacancy diffusion over structure defects like subgrain boundaries or dislocation slip bands, which existed in the sample and were discovered by X-ray topography.

In concluding this section, we give two more examples of pores in aluminum nitride (AlN) and leucosapphire (Al_2O_3). Bulk AlN monocrystals are grown on silicon carbide substrates by the sublimation technique. As is well known, in the cooling of thin ($< 2-3$ mm) crystals obtained on relatively thick SiC substrates, cracks are formed in their volume owing to a large difference in the thermal expansion coefficients of AlN and SiC. In the course of experimental research, it was determined that evaporating the SiC substrate in the course of AlN growth may prevent cracking completely [48–50]. The AlN crystals with the vaporized substrate are practically free of cracks, and at the same time they contain microscopic pores [51, 52]. The kinetics of crystalline silicon carbide evaporation is a complex process, which depends not only on the growth conditions, but also on the geometric dimensions of the crystal, its structural perfection, and crystallographic orientation. Some evaporation features hinder complete substrate removal in the course of AlN growth and favor the formation of pores in it.

Figure 3a shows the phase-contrast image of micropores in a 0.75-mm-thick AlN layer. The pores are hexogonally shaped and have a complex structure, which is made up of boundaries, terraces, tips, and facets. However, the main feature that facilitates their examination is that they are rather large in size, which ranges up to tens of micrometers. This property obviates the need to solve the inverse problem: the pore dimensions can be measured directly on their near-field image.

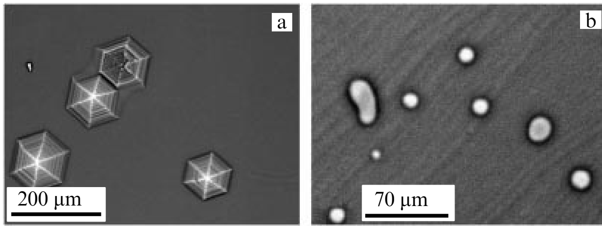

Figure 3. Micropores in AlN (a) and Al_2O_3 (b) monocrystals [39, 49]. (a) Pink SR beam, near field: $r_d = 15$ cm. (b) Monochromatic radiation with energy $E = 25$ keV and energy resolution $\Delta E/E = 0.01$. Far field: $r_d = 25$ cm.

Figure 3b, conversely, shows micropores of a far smaller size. They are gaseous inclusions in shaped sapphire crystals grown by the Stepanov method [53, 54]. Gas bubbles impair the strength of sapphire and exert an adverse effect on its optical and electrical properties. Knowing their nature, it is possible to determine the growth conditions whereby the formation of microbubbles is controlled. In-line phase-contrast imaging holds great promise for determining the size, shape, and density of gas inclusions in the bulk of Al_2O_3 crystals. The microbubble image quality improves under far-field conditions, and therefore they invite the use of two-dimensional simulation methods.

3. Theory of in-line phase-contrast imaging technique with synchrotron radiation

The method of in-line X-ray phase-contrast imaging of transparent objects corresponds almost completely to the idea of holography introduced by Gabor back in 1948 [16]. The idea of the method is simplest to explain with the image of an optical fiber made up of a tungsten wire 15 μm in diameter, on which amorphous boron is deposited in such a way that the total fiber diameter is equal to 100 μm. This object is often employed to determine the spatial coherence of X-ray radiation [55–57].

The setup and results of the experiment are shown in Fig. 4. The real setup also comprises a monochromator, which separates out a narrow peak at a given frequency but does not affect the ray paths and is therefore not shown. The SR source has a finite size S in the direction of the x-axis perpendicular to the optical axis (the z-axis). At a long distance r_s (30–100 m) from the source is the object — the fiber, which absorbs the X-ray radiation only slightly. And placed at a final distance r_d (0.1–5 m) from the object is a position-sensitive detector (a CCD array), which measures the radiation intensity.

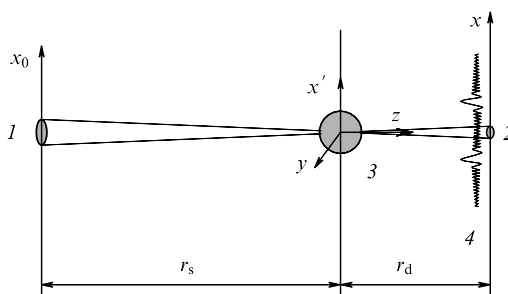

Figure 4. Simplified experimental setup and results in in-line phase-contrast imaging with synchrotron radiation (SR) [56]. *1* — SR source (its transverse size is shown), *2* — transverse size of the source projection on the detector, *3* — sample (fiber), *4* — intensity distribution on the detector.

In the near field, i.e., at a short distance from the object, the interference pattern formation may be qualitatively explained as follows. Due to refraction of the rays at the fiber boundaries, they deviate beyond the shadow region, since the refractive index $n = 1 - \delta$ is smaller than unity. The rays that pass by the object also arrive in this region. Both types of rays find themselves in the detector in the same place and interfere. The phase difference between them varies with a variation in the x-coordinate on the detector due to the different path lengths in the air. As a result, the varying intensity curve shows a maximum when the phase difference is equal to an even integer of π, and a minimum when it is equal to an odd integer of π.

The intensity oscillations are simple in shape but vary in amplitude and period, both the amplitude and period decreasing slowly with distance from the shadow boundary. But the real pattern will depend significantly on the transverse size of the source. True SR sources are point electrons which spontaneously radiate wave trains of a finite length. A good approximation of this source is the model in which every point of the transverse source size radiates independently (incoherently), and the radiation intensity obeys the Gaussian law, i.e., the source may be characterized by its transverse halfwidth.

Every point in the source will produce the same interference pattern (hologram), yet shifted in the transverse direction. This result is easy to obtain simply by turning the optical axis by some angle. Accordingly, the real pattern is obtained from the interference pattern for a point source by convolution with the curve of the source intensity projection on the detector. This is also a Gaussian function of halfwidth $s = Sr_d/r_s$, though. For a relatively small source size S, only distant short-period oscillations vanish. However, with increasing source size, all oscillations may vanish, and the fiber image will disappear, to say nothing of the very weak intensity change due to absorption.

It is significant that the interference nature of the image increases the peak intensity by a factor of four in the maxima closest to the shadow border, while absorption may only decrease the intensity from unity to zero, but for transparent objects the change may amount to a fraction of one percent. It is also important that strong side oscillations are produced by practically all objects of finite size, and not only fibers. And these oscillations do not vanish, even for a relatively large source size [58]. At the same time, it is clear: what matters is the angular source size $\alpha = S/r_s$ on the object rather than the source size itself. This parameter is related to another parameter termed the transverse coherence length $L_{tc} = \lambda/2\alpha$, where λ is the monochromatic radiation wavelength. It is equal to the longest distance between the points in the transverse section of the object which may still interfere.

This method was first proposed and experimentally demonstrated in Refs [22, 23], both of which were carried out on the third-generation SR source in Grenoble, France (ESRF), shortly after it started operating in the first half of the 1990s. At that time, it was the only such source in the world. By the time this review was completed, the Google Scholar service showed 1400 papers that cited Snigirev et al. [22]. Evidently, almost all of these papers deal with the application of the phase-contrast technique in material science, biology, medicine, and other fields.

If we count the yearly citations of this paper, we will see that the numbers increase with time, the number of citations made during the second decade after the publication being much greater than during the first. This is easily explained by the increase in the number of third-generation sources in the world during this period and by the practical significance of the method, especially for biology in the nondestructive investigation of the soft tissue of living organisms. SR rays pass through the object and permits recording the internal structure of the object from the total phase shift along the ray paths in the object. Using the now standard tomography technique [59], in the rotation of the object about the vertical axis it is possible to obtain the two-dimensional electron density distribution in each horizontal section of the sample and even the three-dimensional one from the set of all sections obtained by varying the height of the sample position.

It is impossible to describe all the studies in one review. And so here we mention only those papers in which experimental investigations are accompanied by computer simulations of phase-contrast images and which discuss the development of direct methods to solve the inverse problem of calculating the phase-shift profile in the object from the intensity profile recorded by a detector and employ tomographic methods. Among the wealth of papers of the former type we mention Refs [22, 23, 60–69]. Papers of the latter type [70–101] began to appear simultaneously with experimental investigations, i.e., beginning in 1995, and these investigations continue up to the present time. The situation with the use of tomography is the same. The first paper on tomography [102] appeared in 1996, and the inverse problem was not yet being solved in it, and use was made of the effect of detection of the object domains with different electron densities, which was described above. In subsequent papers [103–118], tomography was done using the phase-shift profile, and the theoretical methods of this tomography were developed.

Simpler formulas result in the one-dimensional version of the theory, when the electron density in the object varies only in the direction of the x axis. The passage to the two-dimensional version is attended by the addition of another variable y in the formulas. Let us consider the one-dimensional version. In the theory of X-ray phase contrast, the paraxial optics approximation provides high accuracy: the longitudinal distances (along the z axis) are measured in centimeters, while the transverse distances (along the x axis) are measured in micrometers, and the radiation wavelength in Angstroms (0.1 nm). Interestingly, when use is made of these units, the formula for the first Fresnel zone $r_1 = (\lambda z)^{1/2}$ does not contain additional factors.

Outlined below are the main propositions of the theory, which are used in many of the papers cited above, and so the references are omitted. This approach is quite general and applies not only to the near field, where the geometrical optics hold good, but also to the far field, i.e., away from the object, where the geometrical optics are inapplicable.

The solution of the Maxwell equation for the electric field of the radiation is found as

$$E(x, z, t) = \exp(\mathrm{i}kz - \mathrm{i}\omega t)\, A(x, z)\,, \tag{2}$$

where $k = \omega/c = 2\pi/\lambda$ is the wavenumber, ω is the radiation frequency, c is the speed of light, and $A(x, z)$ is a slowly varying function (in comparison with the exponential function), which depends on ω as an external parameter. In the paraxial approximation, the equation for this function may be written in the form

$$\frac{\partial A}{\partial z} = -\mathrm{i}k\eta\rho(x, z)A + \frac{\mathrm{i}}{2k}\frac{\partial^2 A}{\partial x^2}\,. \tag{3}$$

Here, $\eta = \delta - \mathrm{i}\beta = 1 - n = -\chi/2$, where n is the complex refraction coefficient, which also takes into account the radiation absorption in the medium, $\chi = \varepsilon - 1$ is the susceptibility of the medium, and ε is the permittivity.

Formula (3) was written under the assumption that the radiation passes through a medium which has the same electron density at points where there is substance, and function $\rho(x, z) = 1$ there, but this function is equal to zero at points where there is no substance. In the case under consideration, the samples are thin in comparison with the very long paths in front of and after the sample. For short paths, we may take advantage of a simplified version of geometrical optics and ignore the bending of ray paths inside the sample. This is an approximation, whereby the second term on the right-hand side of Eqn (3) may be disregarded. After this, the equation is easily solved and the solution has the form

$$A(x, z_1) = A(x, z_0)\, T(x)\,, \quad T(x) = \exp\left[-\mathrm{i}k\eta t(x)\right], \tag{4}$$

where

$$t(x) = \int_{z_0}^{z_1} \mathrm{d}z\, \rho(x, z)\,. \tag{5}$$

Function $T(x)$ is termed the sample transmission function, and function $t(x)$ is the variable sample thickness in the path of the ray directed along the optical axis and deflected to the coordinate x. When the sample is of varying shape or contains voids inside, this function becomes variable. Generally speaking, the transmission function changes both the amplitude and the phase of the wave field. In this case the sample thickness does not enter the problem explicitly, but it should be included in the calculation of the path lengths.

When the free-space paths in front of and after the sample are long, the first term on the right-hand side of Eqn (3) is absent. In this case, the solution may be written in the form of a convolution, namely

$$A(x, z_1) = \int \mathrm{d}x'\, P(x - x', z_1 - z_0)\, A(x', z_0)\,, \tag{6}$$

where the known wave function is used at the input, the result is calculated between infinite limits, and the second function is the Fresnel propagator as the transverse part of the spherical wave in the paraxial approximation:

$$P(x, z) = \frac{1}{(\mathrm{i}\lambda z)^{1/2}} \exp\left(\mathrm{i}\pi\, \frac{x^2}{\lambda z}\right). \tag{7}$$

Formula (6) is the special case of the Huygens–Fresnel principle.

For the simple experimental arrangement depicted in Fig. 4 and for the case of a point source displaced by a distance x_0 from the optical axis, the formula for the wave field amplitude at the detector may immediately be written as

$$A(x, x_0) = \int \mathrm{d}x' P(x - x', r_\mathrm{d}) T(x') P(x' - x_0, r_\mathrm{s})\,. \tag{8}$$

The detector measures the intensity $|A(x)|^2$, but we are interested in function $t(x)$, which is defined by expression (5) and is easily found from the phase of transmission function $T(x)$. Formula (8) and its two-dimension analogue are employed for simulating experimental phase-contrast images on computers. In doing so, the resultant intensity should be convolved with the source intensity function and summed over the possible radiation spectrum.

In several cases, direct methods to solve the inverse problem permit calculating the phase of the transmission function directly from experimental data. Prior to reviewing these methods, we will show that formula (8) may be transformed into another form by separating out the field wave function at the total distance and considering the field ratio between the cases with and without the sample:

$$\frac{A(x,x_0)}{P(x-x_0,r_t)} = a\left(\frac{r_s}{r_t}\left(x + x_0\,\frac{r_d}{r_s}\right)\right), \qquad (9)$$

where

$$a(x) = \int \mathrm{d}x'P(x-x',r')T(x')\,. \qquad (10)$$

Here, $r' = r_d r_s/r_t$ and $r_t = r_s + r_d$. Formulas (9) and (10) explicitly show the symmetry properties of the images obtained by this method.

In particular, the point source displacement by a distance x_0 results in the displacement of the picture as a whole by a distance $-x_0 r_d/r_s$. This property permits the real source size to be taken into account in calculations with relative simplicity. On the other hand, one can see that the resultant pattern is similar to the case of incidence of a plane wave ($r_s = \infty$), irrespective of the source–sample distance. However, in a diverging wave, the resultant pattern is effectively broader and corresponds to a shorter distance than with the parallel beam.

When the sample is finite in size, function $T(x)$ is equal to unity outside it. For this reason, it is convenient to use another formula in calculations instead of expression (10):

$$a(x) = 1 + \int \mathrm{d}x'P(x-x',r')\big[T(x')-1\big]\,, \qquad (11)$$

in which the integral is taken between finite limits and explicitly describes the phase contrast relative to the unit background. Here, use was made of the fact that the integral of the Fresnel propagator is equal to unity.

Although in different publications direct methods to solve the inverse problem are derived in different ways, they all may be derived from integrals (10) and (11). As already noted, the method under consideration is analogous to the Gabor holographic method, and there is a wealth of papers dedicated to the reconstruction of Gabor holograms, including in visible light optics. Gabor holograms are best reconstructed for samples of small transverse size by the method of inverse transformation for the squared modulus (11) [74]. We denote the convolution with the symbol $*$ and introduce the notation $H(x) = |a(x)|^2$, $o(x) = T(x) - 1$. Then,

$$\begin{aligned} R(x) &= P^*(x-x',r') * [H(x')-1] \\ &= o(x) + P^*(x-x',2r') * o^*(x') \\ &\quad + P^*(x-x',r') * \big|P^*(x'-x'',r') * o(x'')\big|^2\,. \end{aligned} \qquad (12)$$

Hence, it is clear that a transformation of this type may be expressed as the sum of three terms. The first is the object image per se. This is the transmission function, from which the phase profile may be obtained. The second term is called the twin image. It somewhat distorts the initial image but not completely, because it is larger in size, as it corresponds to the double distance. And the third term is usually strongly blurred and is a weakly nonuniform background. When the object is well localized, it is discernable.

However, this method is not always efficient for transparent objects. Another way to solve the inverse problem is the iterative method. For transformation (10), it is possible to obtain the inverse transformation

$$T(x) = \int \mathrm{d}x'P^*(x-x',r')a(x')\,. \qquad (13)$$

Measured in experiments are the moduli of functions $T(x)$ and $a(x)$. The task is to calculate their phases. One may start from an arbitrary function and assign it some phase, even the zero one. Upon calculation in one direction, the modulus is replaced for the known one, but the calculated phase is retained. The same is repeated in the calculations in the other direction and so on.

Numerical experiments show that this process converges in several cases and yields correct solutions. At a long distance r', the integral transformation with the Fresnel propagator is equivalent to the Fourier transform. For this transformation, the iterative method was first proposed by Gerchberg and Saxton [119]. They showed this method always provides convergence to the correct solution for objects with a two-dimensional cross section of small size. It underlies the ptychography method [120].

We also mention other approaches. For instance, when the phase of the transmission function is small, we may expand the exponent into a power series and keep only the first expansion term. In this case, the phase profile may be approximately calculated directly from the intensity profile [91]. In a large number of papers, use is made of the so-called intensity transport approximation, which works well at short distances from the sample, i.e., in the near field. When the phase of the transmission function varies slowly, it is possible to obtain the equation relating the intensity profile to the second derivative of the phase.

Alternatively, this approximation may be obtained by calculating integral (10) by the method of stationary phase. Interestingly, this method does not require a high radiation spatial coherence, and it may be applied even for strongly smoothed images. Furthermore, for a high coherence and fast edge oscillations, this method yields satisfactory results only after averaging these oscillations [74].

4. Experimental studies of micropipes in silicon carbide single crystals by the phase contrast method

Although in-line phase-contrast imaging with SR is noted for the simplicity of its basic experimental setup, in reality, the technical means that provide imaging are highly sophisticated and are equipped with an automatic control system. A typical arrangement of experimental equipment is shown in Fig. 5. The sample (a crystal plate P) is located at a distance r_s from the SR source (not shown in the drawing). In the absence of optical elements that provide the time coherence of the beam,

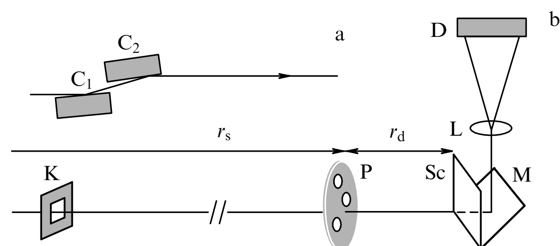

Figure 5. Experimental setup for in-line phase-contrast imaging with SR. (a) Crystal monochromator is tuned to 111 reflection from two silicon crystals C_1 and C_2. (b) Without a crystal monochromator, the SR beam is formed with a slit K and, on passing through a micropore-containing sample P, arrives at the recording system, which consists of a scintillator Sc, a mirror M, a lens L, and a CCD detector D. The SR source and the detector are at respective distances r_s and r_d from the sample.

it passes through the system of slits depicted schematically with one slit K, X-rays pass through the sample, and excites the glow of a crystal scintillator Sc in the visible region. The scintillator is part of the recording system, which also comprises a mirror M, an optical objective L, and a CCD detector D. This way of recording, i.e., projecting the magnified luminescene image onto a CCD, was first employed by Busch and Bonse [121].

The image quality depends on several factors: the scintillator material and thickness, the focal length of the objective, the detector dynamic range, and the CCD-matrix pixel size. A typical drawback of crystal scintillators of compounds like CsI, $CdWO_4$, and $Y_3Al_5O_{12}(Ce)$ is the nonproportionality in response for a certain energy [122]. A large scintillator crystal thickness lengthwise of the beam lowers the resolution, while for a small thickness the scintillator service life is short. Improving efficiency and detection system resolution is the concern of many papers (see, for instance, Refs [123–125]). In these papers, it is common practice to mention the optimized resolution for an effective pixel size, which is equal to the quotient resulting from the division of the real CCD-matrix pixel size by the objective magnification and is less than a micrometer. However, for a submicrometer pixel size, the resolution increases, but the image sharpness deteriorates.

Another important factor which affects image quality is the parasitic noise recorded by the detector. This noise is strongest in a setup without a monochromator (Fig. 5b). The radiation spectrum in this scheme is quite broad, and this radiation is usually termed a 'pink beam'. The pink beam appears in a natural way. As is well known, with a decrease in photon energy, the spectral SR intensity decreases due to absorption in all objects in the beam path, including the sample. And with an increase in energy, the SR intensity decreases monotonically. That is why the radiation spectrum behind the sample has the shape of a peak. In the in-line setup, the frequency variation has only a slight effect on the ray paths but changes the intensity distribution pattern due to the different phase incursion in the sample. The real pattern also depends on the transverse coherence length L_{tc}. Narrowing the spectral peak has a positive effect on the image quality. Extraction of the spectral peak at a given frequency is effected by crystal monochromators made of high-perfection silicon (Fig. 5a) or by X-ray mirrors of synthetic materials [126, 127].

We estimate the longitudinal coherence length L_{lc} for the three cases considered above. For a pink beam, when the total electron energy is equal to 2.5 GeV, the spectrum of radiation from a bending magnet decreases monotonically in the interval between 5 and 40 keV. The inclusion of absorption in the beryllium window and especially in the sample results in a major intensity decrease in low-energy photon radiation. For instance, for a 0.49-mm-thick SiC plate, the FWHM (full width at half maximum) of the spectral peak localized near an energy $E = 16$ keV is $\Delta E = 11$ keV [128]. The longitudinal coherence length is defined by the formula $L_{lc} = hc/\Delta E$, where h is the Planck constant and c is the speed of light [129]. For a pink beam, it is very short: $L_{lc} = 1.1$ Å. In the reflection from a mirror, the FWHM of the spectral peak decreases strongly in comparison with the pink beam. For $\Delta E/E = 4 \times 10^{-3}$, we obtain $L_{lc} = 194$ Å. For a two-crystal Si(111) monochromator, $L_{lc} = 800$ Å for the same energy E of the radiation from a bending magnet [130].

On third-generation SR sources with a total electron energy of 2–2.5 GeV and an electron beam current of ~ 300 mA, bending magnets provide a high intensity only for a pink beam. Even a mirror with an average energy resolution of $\sim 10^{-3}$ attenuates the photon flux so strongly that exposure times may increase by a factor of 20. This lengthens the experiment times significantly, especially for the tomographic technique. According to the most conservative estimates, recording a series of 500 projections will require a time lengthening by a factor of 10^4.

For detectors that measure images in a pink SR beam, useful signals should be significantly stronger than the background, preferably several dozen times stronger. That is why the exposure time should be selected so as to obtain the highest possible intensity, i.e., a 16-bit detector is preferred. A detector with a 12-bit range is better suited for recording monochromatic radiation, which offers the great advantage of very low parasitic scattering. For a detailed description, the reader is referred to the paper by Argunova et al. [39].

Apart from the signal-to-noise ratio, care should be taken with the effective pixel size of the CCD matrix. Let us compare the capabilities of two detectors, M_1 and M_2, with the respective pixel sizes of 5.5×5.5 and 9×9 μm. Let us assume that measurements are made of a micropipe several micrometers in diameter. The image quality depends on the pixel-to-object size ratio. Using a 20× optical lens decreases this ratio, so that image scaling makes the effective pixel size equal to 0.27 and 0.45 μm for M_1 and M_2, respectively. In the near field, where the image size is almost equal to the object size, detector M_1 is preferred to M_2. Both detectors are well suited to measurements in the far field, where the image size is larger. In reality, the real pixel size is larger than the effective one, and the detector resolution is worse than the expected resolution.

Best suited for determining the micropore size in a volume of SiC monocrystals are direct-observation X-ray methods, namely diffraction topography and phase radiography. In both methods, the real size may only be determined by solving the inverse problem, and only the latter method is characterized by sensitivity exclusively to the microobject size and shape. We will show this by comparing the data obtained for dislocated micropipes.

Figure 6 shows X-ray topograms measured in white SR in the Laue geometry from samples with $(11\bar{2}0)$ surface orientation, which were prepared of two different crystals of the 6H-SiC polytype [131, 132]. In the sample with a low defect density, the images of screw superdislocations have smooth edges (Fig. 6a). However, for a high defect density,

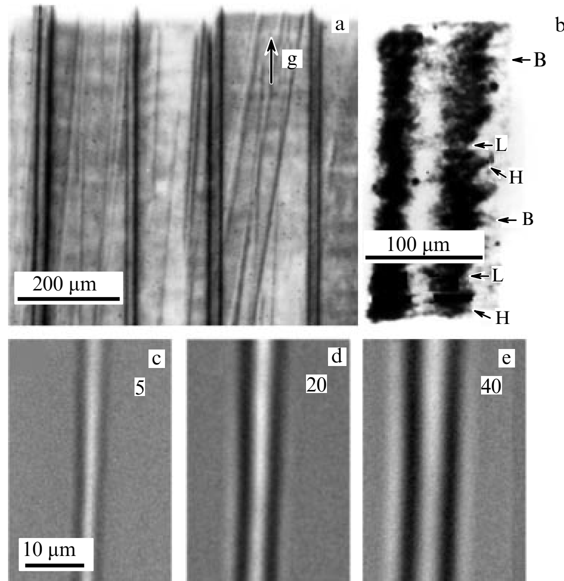

Figure 6. (a) X-ray topogram in transmission geometry, which shows screw superdislocations in a 6H-SiC $(11\bar{2}0)$ monocrystal. Reflection: $g = 0006$ [131]. (b) Topogram of a superdislocation surrounded by populations of basal plane dislocations clusters. The $g = \bar{1}2\bar{1}0$ diffraction vector is directed to the left ($\lambda = 0.64$ Å). Markers B, H, and L indicate regions of different contrast [132]. (c–e) Phase-contrast images of a micropipe measured for different distances between the 4H-SiC $(\bar{1}100)$ sample and the detector [152]. The distances in centimeters are indicated with figures in the images. Main wavelength $\lambda = 0.775$ Å.

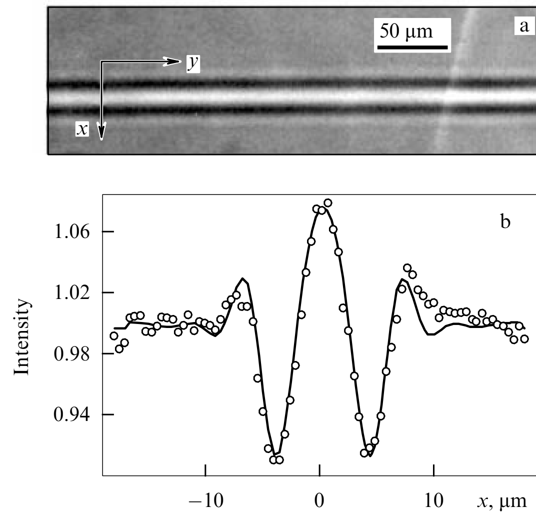

Figure 7. (a) Phase-contrast micropipe image in a pink SR beam. $E = 16$ keV, $\Delta E = 11$ keV. The sample–detector distance $r_d = 40$ cm [39]. (b) Experimental intensity profile (circles) and best-fit theoretical curve (solid line).

their shape is distorted (Fig. 6b). The image structure of a superdislocation whose axis passes inside an MP is highly complex. It is determined by contrast of three types [133]: the bright middle and dark edges are formed due to orientation contrast; the intensity distribution outside the dark edges is due to extinction contrast; and the dynamic contrast merges with the background of the image.

The Burgers vectors of superdislocations were determined by orientation contrast simulations (Fig. 6a) [131]. It was determined that basal plane superdislocations can unite in populations that surround superdislocation cores [132]. The images of dislocations in these aggregates are not resolved as separate lines in topograms. An increase or decrease in their density entails a rise in or lowering of contrast (Fig. 6b). Evidently, the dislocation micropipe images on topograms are entirely determined by the distribution and magnitude of lattice microdistortion rather than by the micropipe morphology.

Figures 6c–e show the phase-contrast images of a portion of one MP recorded at different distances r_d from the sample. The figures in the images indicate the distance in centimeters. At a short distance $r_d \leqslant 5$ cm, the MP image is of the form of a bright band of relatively low contrast (Fig. 6c). With increasing distance, the image structure changes: the bright band widens, and dark bands appear along its edges (Fig. 6d), as do additional bright bands (Fig. 6e). We notice that the transverse pipe size decreases monotonically from top to bottom in the image obtained at a distance of 5 cm.

In the near field, the image size correlates with the true cross-section dimension, and it may be inferred that the cross section of this MP does vary along its axis. Interestingly, for $r_d = 20$ cm, the variation of the spacing between the dark bands is hardly noticeable, while for $r_d = 40$ cm, this spacing appears to be invariable. Only the image contrast varies. This effect is explained below. A comparison of topography and phase-radiography data in Fig. 6 is in favor of the latter as regards determination of microobject sizes. However, it will be shown (see Section 5) that the phase-contrast image of an object recorded at various distances first increases and, second, changes its structure. The solution to the inverse problem calls for determining the mechanism of these changes.

A quantitative analysis of the experimental data was made using a computer image simulation program [128, 134–136]. The program is described in Section 5. We apply the program to determine the section size of an MP. Figure 7a depicts a part of the image recorded in a pink SR beam ($L_{tc} = 21$ cm) [39]. The sample in the form of a 490-μm-thick plate of orientation $(\bar{1}100)$ was cut from a 4H-SiC crystal grown by the sublimation method [137] in the direction $\langle 0001 \rangle$ and carefully polished on both sides. The MP axes were parallel to the plate surface. The sample was aligned perpendicular to the beam in such a way that the micropipe axes were horizontal. The circles in Fig. 7b show the normalized experimental intensity values measured at a distance $r_d = 40$ cm across the MP axis using the ImageJ code [138].

Specified as the first approximation was the model of an elliptically shaped cross section. The program fitted the experimental intensity profile by automatic variation of the initial values of the transverse D and longitudinal D_0 diameters in the direction perpendicular and parallel to the beam, respectively. The broad radiation spectrum was taken into account in the calculation by summing up the images for the monochromatic harmonics with weights corresponding to the real SR spectrum, which was measured by the detector. The program calculated by itself the radiation spectrum with the inclusion of all absorbers in the beam path, including the sample. By gradually changing the initial model, the best fit to the experimental curve was obtained for $D = 1.36$ μm and $D_0 = 1.82$ μm. The theoretical intensity profile corresponding to the least squares sum $\chi^2_{\min} = 9.8 \times 10^{-5}$ is plotted in Fig. 7b with a solid line.

To make certain that the resulting cross section diameters are correct, one has to fit the images of the same MP at

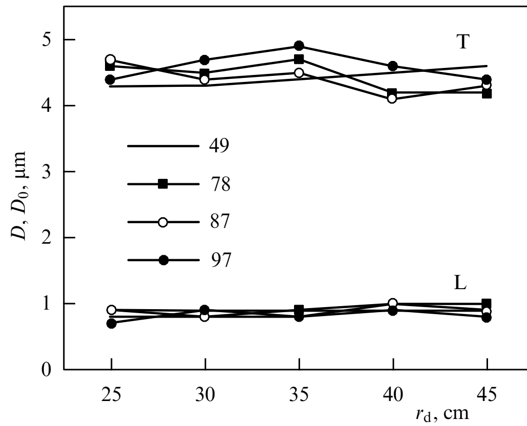

Figure 8. Diameters D and D_0 determined for four cross sections along one MP in relation to the sample–detector distance r_d. The positions of the cross sections in micrometers are indicated in the plot. T — transverse (D) and L — longitudinal (D_0) diameters [135, 136].

different distances r_d. In this case, the real cross section size should not depend on the distance. The validity of this statement guarantees the correctness of experiment formulation and simulation procedure. Plotted in Fig. 8 are the dependences of the cross section sizes on the distance r_d for four close sections [135, 136]. Although the data do not lie in one line, it can be seen that the resultant parameters change only slightly with distance and along the pipe axis. The transverse and longitudinal diameters D and D_0 nevertheless differ markedly for these cross sections: D_0 is equal to only 0.8–1 μm, while the transverse diameter is equal to 4.5–5 μm. This experimental result turned out to be quite unexpected.

In the theory of elasticity, the elliptic cross section of an MP was predicted earlier. Analyzing the models of equilibrium morphology of hollow superdislocation cores, the authors of Ref. [139] found that, first, round pipes about screw dislocations predicted by Frank [4] are stable in an isotropic material; second, the pipes about edge dislocations are also stable, but they are not round, even in an isotropic material. The hollow cores of edge superdislocations have an elliptical shape determined by the symmetry of the elastic field of these dislocations. Hirth [140] calculated the elastic fields for both edge and screw dislocations with a hollow core elliptical in shape.

Returning to the simulation results, we note that the unusual MP cross section shape strongly elongated across the beam was also observed for many other MPs [39, 141, 142]. In accordance with the experimental observations made by other methods — polarization optical microscopy [143, 144] and TEM [11] — as well as with the statement that growth steps and MPs may be caused by the dislocations of mixed or even of purely edge types [145], one might expect that the superdislocations inside the pipes of an elliptical cross section are not screw ones. However, considering that pipes of unusual shape were observed in the regions of defect accumulation (at the boundaries of pores or inclusions of other polytypes), this would be difficult to prove by X-ray methods. The use of X-ray topography for analyzing dislocations in the regions of dense defect accumulation did not provide an unambiguous answer to this question [141]. To explain the MP elliptical cross section and the variation in its size along the axes of some MPs, the authors of Ref. [142] proposed a model of dislocation-to-MP transformation due to the nonequilibtium processes of pipe diffusion and vacancy coagulation at the dislocations parallel to the crystal growth axis.

We note that MPs change in the course of crystal growth. This complicated effect comprises the formation of new MPs [7, 11–13], MP dissociation with the production of dislocations [146–148], interaction with the inclusions of other polytypes [35, 36], etc. Figure 9a shows an optical microphotograph of the growth surface of the 4H-SiC epitaxial layer deposited on a substrate of the same polytype [146]. Prior to the observation, the sample was etched in a solution of KOH. Two kinds of etching pits appeared in the same place where there was one large pit on the substrate (Fig. 9b). Dark pits hexagonal in shape are dislocation MPs; round pits correspond to elementary screw dislocations. This is an indication that the MP grew into the layer, and screw dislocations were formed in the course of epitaxy. During subsequent growth, the pipe was overgrown.

Another example — the splitting of one MP into two MPs with a smaller diameter — is seen in Figs 9c and 9d. Two etching pits on the 4H-SiC crystal surface revealed by the SEM method (Fig. 9c) correspond to two MPs in the crystal volume (Fig. 9d), which were produced by splitting, as shown by phase-contrast imaging with SR [149].

In Section 2, we listed reactions between dislocated MPs, which occur when pipes come into contact and touch each other at their surfaces. These contact reactions may effectively decrease the MP density distribution. However, as the density lowers, they become progressively less probable. Dislocation MPs nevertheless continue to interact at a distance, now in a contact-free way. This new form of MP evolution was discovered thanks to the method of phase-contrast image simulation. The method made it possible to reveal the correlated variations of the transverse sections of two neighboring MPs along their axes. The basic idea which explains this observation is that the MPs can interact by exchanging dislocations [134]. A mechanism of contact-free interaction was developed, which may result in a decrease in their cross sections and in the overgrowing of the MPs [150, 151].

Experimental data which serve to demonstrate the cross section size variation are shown in Fig. 9e. In the phase-contrast image, the two MPs at the top are in contact, while the third MP is away from them. The transverse diameters of each pipe determined with a simulation program in its various sections are shown with square and round markers for MP1 and MP2, respectively [134, 150]. The marker positions correspond to the cross section positions, and their transverse diameters are indicated by figures. The growth direction is indicated with an arrow pointing to the left. As is clear from Fig. 9e, the transverse pipe sizes change sharply with crystal growth.

As this takes place, the following correlation is observed between the changes. For MP1, the transverse size decreases sharply from 7.4 to 5.3 μm over the interval from 329 to 280 μm along its axis, while for its neighboring MP2 the size reduction from 3.7 to 1.8 μm occurs slightly later over the interval from 89 to 58 μm. Since the cross section of an MP is related to its Burgers vector by Frank's formula [4], the observed effect is attributable to reactions between the dislocations. During crystal growth, one micropipe (MP1) emits a dislocation loop, which expands, reaches the surface of the other micropipe (MP2) and reacts with its dislocation. In this case, the signs of the Burgers vectors of screw

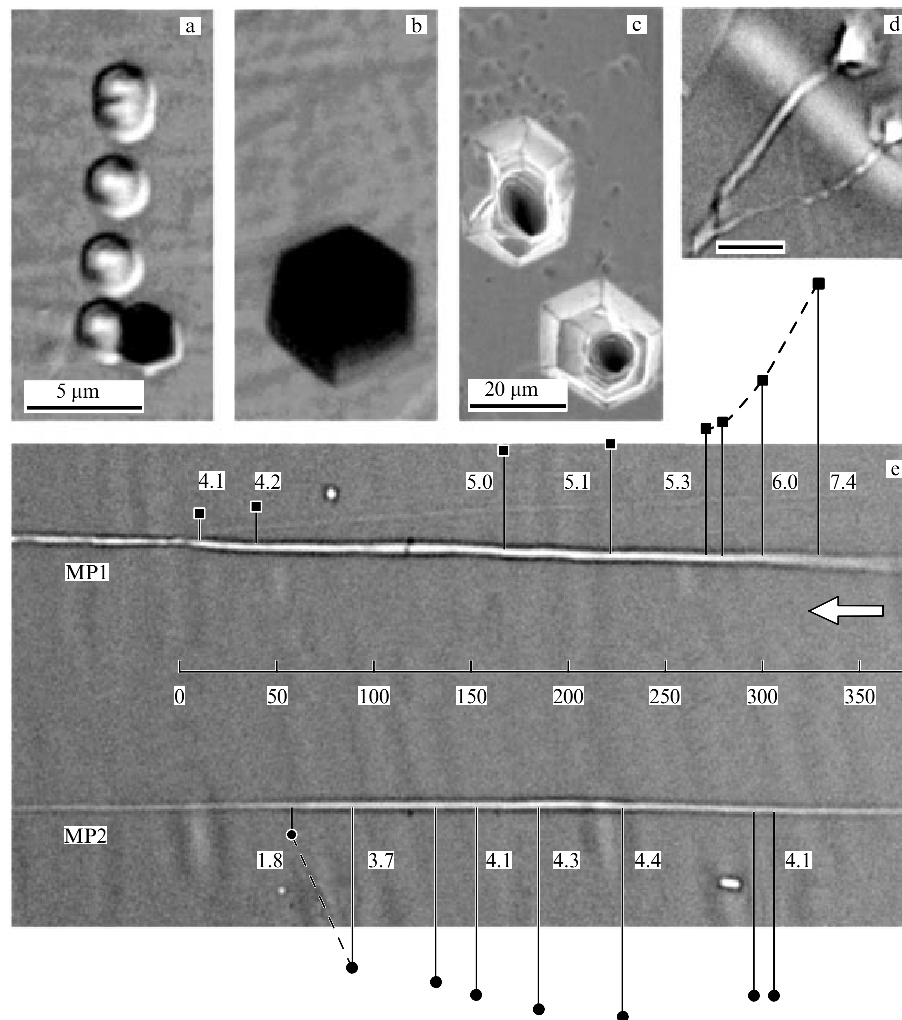

Figure 9. Reactions of dislocated micropipe splitting into dislocations (a, b) [146] or into two other micropipes (c, d) [141]. The scale bar, 50 μm (d). (e) Correlated variations of the cross sections of two neighboring micropipes along their axes [150]. The length units are in micrometers.

dislocations MP1 and MP2, as well as of the absorbed loop segment, may be such that both MPs decrease in diameter.

A comparison of the nondestructive research methods outlined in this section suggests that the in-line phase-contrast imaging ranks as high as — and in some cases exceeds — the capabilities of each of the other methods, like topography, SEM, and optical microscopy, for determining the morphology and sizes of micropores in monocrystals. However, quantitative information cannot be obtained by the phase-contrast method without solving the inverse problem. Computer simulation of the images, which is developing in parallel with and yet independently of the methods for phase retrieval, is not sufficiently advanced. Nevertheless, the application of the in-line method to meet the demands of material science is coming to be a commonly accepted practice.

In the future, major achievements would be expected to be made due to the increase in brightness of SR sources on storage rings and improvement in radiation detector technologies. At present, medium-brightness sources are being upgraded almost everywhere to raise the electron energy in the storage ring. The use of undulators and wigglers on sources with a total electron energy of 3 GeV and an e-beam current of 300–400 mA entails a significant increase in radiation intensity and hardness. Evidently, broadening the capabilities of phase radiography and tomography calls for further improvement in the brightness of SR sources.

5. Computer simulation of images and inverse problem solution

As noted in Section 4, in a large number of studies, images of micropipes in SiC were obtained in experiments with a pink beam, which had a very low temporal coherence. For a low temporal coherence, the image details located away from the center vanish, but the central part of the image is nevertheless retained. Furthermore, the small diameters of MP cross sections (from one to several micrometers), as opposed to the effective detector resolution (about 0.5 μm), compel recording the images away from the sample (up to 50 cm away).

According to the optical analogue of the quantum mechanical uncertainty relation, for a wavelength $\lambda = 0.08$ nm, an MP of transverse size $D = 1.6$ μm produces an angular divergence $\theta = \lambda/D = 5 \times 10^{-5}$ for the scattered radiation. In this case, the image size at a distance $r_{\rm d} = 50$ cm is formally equal to $r_{\rm d}\theta = 25$ μm, i.e., signifi-

cantly exceeds the size of the object and may well be recorded by the indicated detector. The coherent far-field image of an MP under restricted beam illumination is the profile of the squared modulus of the Fourier transform of the MP transmission function. In the case under consideration, the beam is not restricted, and the image is strongly distorted by summation over the broad spectral radiation peak. In this case, the images for different wavelengths, broadly speaking, are different, and the summation does not come to the convolution of two functions.

Under these conditions, there is no way of using direct methods to solve the inverse problem of calculating the phase profile from the intensity profile recorded by the detector. However, there always persists the universal method of computer image simulation based on some simplified model of the object. In the MP simulation, it would by natural to consider the MP an empty pipe of elliptical cross section defined by two diameters D and D_0 across and along the beam. Accordingly, the transmission function of this object is equal to 1 for $|x| > R$, and for $|x| < R$,

$$T(x) = \exp\left([\mathrm{i}\Phi + M]\left(1 - \frac{x^2}{R^2}\right)^{1/2}\right),$$
$$\Phi = \frac{8\pi}{\lambda}\,\delta D_0\,, \qquad M = \Phi\,\frac{\beta}{\delta}\,. \tag{14}$$

Here, $R = D/2$ and parameters δ and β are defined by formula (3).

To simulate images in Refs [39, 128, 134–136, 141, 142, 150, 152–157], use was made of the FIMTIM (FItting MTube IMage) code, which calculated a series intensity profiles on the detector for a set of monochromatic radiation wavelengths and a point source in accordance with formulas (7), (11), and (14). The convolution of the Fresnel propagator with the transmission function of the object was calculated by the fast Fourier transform [158]. In this case, the Fourier image of the transmission function was calculated numerically, and the Fourier image of the Fresnel propagator had an analytical expression. The inverse Fourier transform of the product of the Fourier images of the two functions provided the desired solution. The intensity profiles were then distorted in the course of calculation of the convolution with the intensity function in the transverse section of the source and summation of all curves for different wavelengths with weights corresponding to the radiation spectrum, which was calculated with the inclusion of radiation absorption in the MP-bearing crystal. In the calculation of the curve, specific parameter values D and D_0 were specified.

At the next stage, the calculated curve was compared to the experimental curve, which was normalized so as to obtain a unit background. Actually calculated was the total intensity (the sum over all points), which was then divided by the number of points, and all experimental values were divided by the resultant value. The sum of the squared departures $\chi^2(D, D_0)$ of calculated image values from the experimental ones was used for fitting. Determined in this case were such values of D and D_0 that minimized this function. Selecting the central point in the experimental curve was also a certain problem. It was also determined from the minimum-χ^2 condition. Standard methods were employed to search for the minimum point.

The specific character of this problem lay in the fact that it was important not only to find the minimum point but also to check the shape of the minimum so as to get an idea of how accurately the D and D_0 parameters were calculated. To this end, upon finding the minimum point, we calculated the $\chi^2(D, D_0)$ function distribution map in the plane of its arguments near the minimum. It turned out that the contour curves were strongly elongated along the $DD_0 = \mathrm{const}$ hyperbola in the majority of cases. This signifies that the micropipe cross section area was determined with a high accuracy, but each of the diameters was determined with a lower accuracy.

To understand why this is so, in Ref. [152] the problem was solved analytically in the case when the transverse micropipe cross-section diameter $D \ll r_1$, where $r_1 = (\lambda r_{\mathrm{d}})^{1/2}$ is the radius of the first Fresnel zone, and the longitudinal diameter D_0 is so small that phase $\Phi < 0.5$. Then, for monochromatic radiation and a point source, it is possible to derive the following approximate formula for the normalized intensity profile:

$$I(x) \approx 1 + \frac{\pi^2\delta}{\lambda r_1}\,DD_0 b(x)\cos\left(\pi\,\frac{x^2}{r_1^2} + \frac{\pi}{4}\right),$$
$$b(x) = \frac{2x_{\mathrm{c}}}{x}\,J_1\left(\frac{x}{x_{\mathrm{c}}}\right), \qquad x_{\mathrm{c}} = \frac{r_1^2}{\pi D}\,. \tag{15}$$

Here, $J_1(x)$ is the first-order Bessel function.

In the case under consideration, $x_{\mathrm{c}} \gg r_1$. That is why the structure of the image in its central part, where $|x| < x_{\mathrm{c}}$, is determined only by the cosine, which is independent of the micropipe cross-section diameters. That is, the intensity profiles of the MP image are universal in character. And the contrast ratio is defined only by the product DD_0. The intensity distribution curve calculated by the FIMTIM program is plotted in Fig. 7b, with experimental points superimposed on it. The curve shape may be explained with the help of formula (15), although the MP parameters do not perfectly correspond to the necessary condition of its applicability in this specific case.

Namely, the width of radiation scattered by the MP is defined by parameter x_{c}, which is proportional to $r_{\mathrm{d}}\theta$. However, since the beam is not limited to the domain equal to the object in size, intensity oscillations appear, the first maximum having FWHM proportional to the diameter of the first Fresnel zone for a distance r_{d}, which is proportional to $r_{\mathrm{d}}^{1/2}$. This image has the appearance of a bright central zone surrounded by dark zones and further by bright zones again. Images of this type are depicted in Figs 6c–e and 7a. The MP image dimensions nevertheless increase with the sample–detector distance, although not as fast as in diffraction by a slit. As is noteworthy, although the cosine has many oscillations of equal amplitude, after summation over a broad radiation spectrum, only the bright central part and the nearest dark fringes persist. Additional Fresnel zones may be observed only in some images obtained with more coherent radiation.

From the aforesaid, it follows that the micropipe cross-section area may always be determined. The diameters D and D_0 may be determined separately only when the conditions $D \ll r_1$ and $\Phi < 0.5$ are not satisfied. Notably, there is no way of using too long a distance r_{d}, i.e., it is expedient to search for a compromise between the image size and its informativity.

We note that it is impossible to unambiguously determine the real diameters of the MP cross section using one projection. The D and D_0 values obtained with the help of the program should be interpreted by resorting to additional

information. For instance, parameter D_0 is the longitudinal micropipe diameter D_{MP} only when the MP axis is perpendicular to the beam direction, i.e., when angle α between the MP axis and the beam direction is equal to 90°. In the general case, $D_{MP} = D_0 \sin\alpha$. The value of angle α may only be determined by turning the sample 90°. However, in this case the sample thickness will be very large, since the samples usually have the shape of a plate. To gain the possibility of rotating the sample, it should be prepared in a special way.

In (0001) oriented SiC plates, the MPs are aligned almost parallel to the beam direction, and angle α is very small. In this case, parameter D_0 turns out to be very large and $\Phi \gg 2\pi$. In this case, simulations using the program have the result that at the center of such MPs there is a dark fringe, which may be of a different width. Moreover, these dark MP images are indeed observed rather frequently [154]. In the rotation of the sample, their contrast ratio may change and become normal, but in doing this it is clearly seen that they are inclined at a large angle to the rotation axis.

The same problem arises for vertical MPs of elliptical cross section in samples parallel to the growth axis $\langle 0001 \rangle$. The ellipse projection in different directions has different widths, i.e., parameter D corresponds to the width of the ellipse projection in a certain direction, and the maximal phase Φ, which is proportional to D_0, will also depend on the projection direction, because the cross-section area, which is proportional to the product DD_0, persists in the rotation. The lengths of the minor and major ellipse axes may be obtained as the minimal and maximal values of D or D_0 in the rotation of the sample by 180°. And in the rotation by 90°, the values of D and D_0 change places. However, in the investigation of D and D_0, parameter variation along the MP axis this is not very important. The very actuality of this variation may well be recorded for one projection [157].

For micropores with dimensions limited in three directions, for instance spherical voids, the same approach may be employed, though in three dimensions. In this case, the transmission function will depend on two coordinates, x' and y', while the integration in formula (11) should be performed over two variables. Accordingly, one more Fresnel propagator is added, which depends on variables y and y'. The micropore image is formed on the (x, y) variable plane. Such calculations were made in Ref. [156] for monochromatic radiation and capsule-shaped micropores, i.e., for cylinders of limited length. The images resulting from the calculations corresponded nicely to experimental images obtained with both monochromatic and polychromatic radiation. It was hypothesized that the pattern was greatly deteriorated by the low detector resolution, and so the image obtained with monochromatic radiation differed little from the polychromatic image.

Calculations for spherical voids were made in Ref. [39]. As shown there, although the images simulated for the correct radii of spherical voids correspond to the experiment, they have subtle features which the experiment does not reveal, even in monochromatic radiation. In this case, an interesting feature of the two-dimensional experimental images is that the pattern has the same resolution in the horizontal and vertical directions, although the source dimensions in these directions are much different: the horizontal source dimension is several times greater than the vertical one. Furthermore, for a pixel size of 0.25 μm, the image would be sharper and would reveal small details, which are seen in the simulated curves.

This experimental fact has not been reasonably explained so far, and the specific cause of this effect is still unclear. The possible reasons are as follows: the effective detector resolution is much lower than the pixel size estimated from the optical scheme; the vertical source size is small but its position in space may vary with time and increase the effective source size; the monochromator may impair the vertical spatial coherence. In the course of every experiment, it is necessary to carefully investigate the degree of radiation coherence using model samples, which is commonly not done due to limitations on the operating time on SR sources.

6. Conclusions

We have considered various aspects of in-line phase-contrast imaging with synchrotron radiation as applied to measurements of micropore images in silicon carbide monocrystals. After the publication of the pioneering work by Snigirev et al. [22] in 1995, who proposed this method, it has been used extensively in various branches of science. However, a relatively small number of investigations have used this method to quantitatively analyze micropores in monocrystals, and its application to micropores ranging in size from a fraction of a micrometer to several micrometers has never been the subject of a review paper. Our review fills this gap.

For a rather long time, phase-contrast images were only employed for the experimental observation of the state of a substance's microstructure. This approach is exemplified by the study of the micropore nature in quasicrystals, which was carried out by Baruchel's group on the ESRF in Grenoble [159–161]. At the same time, the experimental method may yield quantitative information with the use of theoretical computer simulations and the solution to the inverse problem. Experimental investigations by phase radiography and topography methods have developed into the quantitative analysis of contrasts of near-field images with support from numerical simulations [62].

The method described in our review has become highly popular in eastern Asia, where it initiated the use of X-ray phase contrast at the Beijing Synchrotron Radiation Facility (BSRF) in China, the Pohang Light Source (PLS) in South Korea, and the Taiwan Photon Source (TPS) in Taipei, Taiwan. The relatively simple setup of the method has made it attractive for a variety of purposes. After setting up the sophisticated and massive equipment, researchers study annealing, solidification, melting, deposition, etc. However, adaptation of the method developed on the ESRF (Grenoble, France), i.e., on the best source, to the conditions of medium-brightness sources ran into a serious problem. Initially, the method came into use with a pink beam, i.e., without a monochromator. Significant advances were associated with the study of biomedical objects [162–165] as well as with near-field *in situ* experiments [166]. However, the application of this method to monocrystalline materials for electronic engineering containing microinhomogeneities, for instance SiGe, SiC, and Al_2O_3, revealed its limitations and drawbacks, among which are the simplification and distortion of image structure due to summation over the spectrum. As a consequence, it was impossible to use direct methods to solve the inverse problem. Instead, for relatively simple objects like micropipes, methods were developed to simulate the object by two parameters and determine the parameters by comparing the simulated and experimental images.

The present time is witnessing the passage to experiments with monochromatic SR. This is favored by projects like the reconstruction of the PLS source without its shutdown, the construction of new stations on the TPS and PLS, and the transition to new-generation sources in Shanghai and Pohang. Not only in Asia but also worldwide, phase-contrast imaging has become one of the keys in upgrading programs of almost all major SR sources.

References

1. Kimoto T *Prog. Cryst. Growth Charact. Mater.* **62** 329 (2016)
2. Luchinin V, Tairov Yu *Sovrem. Elektron.* (7) 12 (2009)
3. Lebedev A, Sbruev S *Elektronika. Nauka Tekhnol. Biznes* (5) 28 (2006)
4. Frank F C *Acta Cryst.* **4** 497 (1951)
5. Verma A, Krishna P *Polymorphism and Polytypism in Crystals* (New York: Wiley, 1966); Translated into Russian: *Polimorfizm i Politipizm v Kristallakh* (Moscow: Mir, 1969)
6. Si W et al. *J. Electron. Mater.* **26** 128 (1997)
7. Ma X *J. Appl. Phys.* **99** 063513 (2006)
8. Heindl J et al. *J. Cryst. Growth* **179** 510 (1997)
9. Strunk H P et al. *Adv. Eng. Mater.* **2** 386 (2000)
10. Ma X *Mater. Sci. Eng. B* **129** 216 (2006)
11. Heindl J et al. *Phys. Rev. Lett.* **80** 740 (1998)
12. Dudley M et al. *Appl. Phys. Lett.* **75** 784 (1999)
13. Ohtani N et al. *J. Cryst. Growth* **226** 254 (2001)
14. Eddy C R (Jr.), Gaskill D K *Science* **324** 1398 (2009)
15. Müller St G et al. *J. Cryst. Growth* **352** 39 (2012)
16. Gabor D *Nature* **161** 777 (1948)
17. Weon B M et al. *Int. J. Nanotechnol.* **3** 280 (2006)
18. Nugent K A *Adv. Phys.* **59** 1 (2010)
19. Mayo S C et al. *Materials* **5** 937 (2012)
20. Lider V V, Kovalchuk M V *Crystallogr. Rep.* **58** 769 (2013); *Kristallogr.* **58** 764 (2013)
21. Endrizzi M *Nucl. Instrum. Meth. Phys. Res. A* **878** 88 (2018)
22. Snigirev A et al. *Rev. Sci. Instrum.* **66** 5486 (1995)
23. Cloetens P et al. *J. Phys. D* **29** 133 (1996)
24. Takasu S, Shimanuki S *J. Cryst. Growth* **24–25** 641 (1974)
25. Hawley M et al. *Science* **25** 1587 (1991)
26. Qian W et al. *Appl. Phys. Lett.* **67** 2284 (1995)
27. Valcheva E, Paskova T, Monemar B *J. Cryst. Growth* **255** 19 (2003)
28. Chernov A A *Sov. Phys. Usp.* **4** 116 (1961); *Usp. Fiz. Nauk* **73** 277 (1961)
29. Pandey D, Krishna P *Mater. Sci. Eng.* **20** 243 (1975)
30. Krishna P, Jiang S-S, Lang A R *J. Cryst. Growth* **71** 41 (1985)
31. Tairov Yu M, Tsvetkov V F *J. Cryst. Growth* **52** 146 (1981)
32. Glass R C et al. *J. Cryst. Growth* **132** 504 (1993)
33. Neudeck P G et al. *IEEE Trans. Electron. Dev.* **46** 478 (1999)
34. Huang X R et al. *J. Appl. Cryst.* **32** 516 (1999)
35. Gutkin M Yu et al. *J. Appl. Phys.* **100** 093518 (2006)
36. Gutkin M Yu et al. *Phys. Rev. B* **76** 064117 (2007)
37. Gutkin M Yu et al. *J. Appl. Phys.* **106** 123515 (2009)
38. Gutkin M Yu et al., in *Silicon Carbide — Materials, Processing and Applications in Electronic Devices* (Ed. M Mukherjee) (Croatia: Intech Publ., 2011) p. 187
39. Argunova T S et al., in *Microscopy: Advances in Scientific Research and Education* (Ed. A Mèndez-Vilas) (Badajoz, Spain: Formatex Research Center, 2014) p. 955
40. Gutkin M Yu et al. *Appl. Phys. Lett.* **83** 2157 (2003)
41. Gutkin M Yu et al. *J. Appl. Phys.* **94** 7076 (2003)
42. Gutkin M Yu et al. *Proc. SPIE* **5831** 125 (2005)
43. Argunova T S et al. *Poverkhnost* (8) 59 (2005)
44. Augustine G et al. *Phys. Status Solidi B* **202** 137 (1997)
45. Takahashi J, Ohtani N *Phys. Status Solidi B* **202** 163 (1997)
46. Nakamura D et al. *Nature* **430** 1009 (2004)
47. Mokhov E N, Nagalyuk S S *Tech. Phys. Lett.* **37** 999 (2011); *Pis'ma Zh. Tekh. Fiz.* **37** (21) 25 (2011)
48. Argunova T S et al. *Mater. Sci. Forum* **821–823** 1011 (2015)
49. Argunova T S et al. *Phys. Solid State* **57** 2473 (2015); *Fiz. Tverd. Tela* **57** 2400 (2015)
50. Argunova T S et al. *J. Mater. Sci.* **52** 4244 (2017)
51. Mokhov E N et al. *CrystEngComm.* **19** 3192 (2017)
52. Argunova T S et al. *Crystals* **7** (6) 163 (2017)
53. Denisov A V et al. *J. Cryst. Growth* **344** 38 (2012)
54. Bunoiu O M, Duffar Th, Nicoara I *Prog. Cryst. Growth Character. Mater.* **56** 123 (2010)
55. Kohn V, Snigireva I, Snigirev A *Phys. Rev. Lett.* **85** 2745 (2000)
56. Kohn V, Snigireva I, Snigirev A *Opt. Commun.* **198** 293 (2001)
57. Snigireva I, Kohn V, Snigirev A *Nucl. Instrum. Meth. A* **467–468** 925 (2001)
58. Snigirev A A et al. *J. Synch. Investig.* **1** 1 (2007); *Poverkhnost* (1) 3 (2007)
59. Kak A C, Slaney M *Principles of Computerized Tomographic Imaging* (New York: IEEE Press, 1988)
60. Stevenson A W et al. *Nucl. Instrum. Meth. Phys. Res. B* **199** 427 (2003)
61. Wu X, Liu H *J. X-Ray Sci. Technol.* **11** 33 (2003)
62. Agliozzo S, Cloetens P *J. Microscopy* **216** 62 (2004)
63. Zabler S et al. *Rev. Sci. Instrum.* **76** 073705 (2005)
64. Nesterets Ya I et al. *Rev. Sci. Instrum.* **76** 093706 (2005)
65. Arhatari B D et al. *Rev. Sci. Instrum.* **75** 5271 (2004)
66. Arhatari B D et al. *Rev. Sci. Instrum.* **76** 113704 (2005)
67. Nesterets Ya I et al. *Opt. Commun.* **259** 19 (2006)
68. Nesterets Ya I *Opt. Commun.* **281** 533 (2008)
69. Gureyev T E et al. *Opt. Express* **16** 3223 (2008)
70. Gureyev T E, Roberts A, Nugent K A *J. Opt. Soc. Am. A* **12** 1932 (1995)
71. Gureyev T E, Roberts A, Nugent K A *J. Opt. Soc. Am. A* **12** 1942 (1995)
72. Gureyev T E, Nugent K A *J. Opt. Soc. Am. A* **13** 1670 (1996)
73. Nugent K A et al. *Phys. Rev. Lett.* **77** 2961 (1996)
74. Kohn V G *Phys. Scripta* **56** 14 (1997)
75. Nakajima N *Appl. Opt.* **37** 6219 (1998)
76. Cong W-X, Chen N-X, Gu B-Y *Appl. Opt.* **37** 6906 (1998)
77. Gureyev T E, Wilkins S W *Opt. Commun.* **147** 229 (1998)
78. Tommasini R et al. *Opt. Commun.* **153** 339 (1998)
79. Paganin D, Nugent K A *Phys. Rev. Lett.* **80** 2586 (1998)
80. Gureyev T E et al. *J. Phys. D* **32** 563 (1999)
81. Cheng J, Han S *Opt. Commun.* **172** 17 (1999)
82. Gureyev T E *Optik* **110** 263 (1999)
83. Gureyev T E et al. *Phys. Rev. Lett.* **86** 5827 (2001)
84. Paganin D et al. *J. Microscopy* **206** 33 (2002)
85. Mayo S C et al. *J. Microscopy* **207** 79 (2002)
86. Gureyev T E et al. *J. Synchrotron Rad.* **9** 148 (2002)
87. Suzuki Y, Yagi N, Uesugi K *J. Synchrotron Rad.* **9** 160 (2002)
88. Schelokov I, Weitkamp T, Snigirev A *Opt. Commun.* **213** 247 (2002)
89. Hennelly B, Sheridan J T *Opt. Commun.* **226** 61 (2003)
90. Gureyev T E et al. *Opt. Commun.* **231** 53 (2004)
91. Kohn V et al. *Nucl. Instrum. Meth. Phys. Res. A* **543** 306 (2005)
92. Gureyev T E et al. *Opt. Commun.* **259** 569 (2006)
93. Shioya H, Gohara K *Opt. Commun.* **266** 88 (2006)
94. Marchesini S *Rev. Sci. Instrum.* **78** 011301 (2007)
95. Paganin D M, Gureyev T E *Opt. Commun.* **281** 965 (2008)
96. Langer M et al. *Med. Phys.* **35** 4556 (2008)
97. Kashyap Y S et al. *J. Synchrotron Rad.* **17** 799 (2010)
98. Burvall A et al. *Opt. Express* **19** 10359 (2011)
99. Weitkamp T et al. *J. Synchrotron Rad.* **18** 617 (2011)
100. Diemoz P C et al. *J. Synchrotron Rad.* **22** 1072 (2015)
101. Gureyev T E et al. *J. Opt. Soc. Am. A* **34** 2251 (2017)
102. Raven C et al. *Appl. Phys. Lett.* **69** 1826 (1996)
103. Bronnikov A V *Opt. Commun.* **171** 239 (1999)
104. Spanne P et al. *Phys. Med. Biol.* **44** 741 (1999)
105. Cloetens P et al. *Appl. Phys. Lett.* **75** 2912 (1999)
106. Cloetens P et al. *Proc. SPIE* **3772** 279 (1999)
107. Baruchel J et al. *J. Synchrotron Rad.* **7** 196 (2000)
108. Barty A et al. *Opt. Commun.* **175** 329 (2000)
109. Weitkamp T et al. *Proc. SPIE* **4503** 92 (2002)
110. McMahon P J et al. *Opt. Commun.* **217** 53 (2003)
111. Peele A G et al. *Rev. Sci. Instrum.* **76** 083707 (2005)
112. Zabler S et al. *Opt. Express* **14** 8584 (2006)
113. Groso A et al. *Appl. Phys. Lett.* **88** 214104 (2006)
114. Gureyev T E, Nesterets Ya I, Mayo S C *Opt. Commun.* **280** 39 (2007)
115. Arhatari B D, De Carlo F, Peele A G *Rev. Sci. Instrum.* **78** 053701 (2007)

116. Vagberg W et al. *Sci. Rep.* **5** 16625 (2015)
117. Baran P et al. *Phys. Med. Biol.* **62** 2315 (2017)
118. Nesterets Ya I, Gureyev T E, Dimmock M R *J. Phys. D* **51** 115402 (2018)
119. Gerchberg R W, Saxton W O *Optik* **35** 237 (1975)
120. Pfeiffer F *Nature Photon.* **12** 9 (2018)
121. Bonse U, Busch F *Prog. Biophys. Molec. Biol.* **65** 133 (1996)
122. Dorenbos P et al. *IEEE Trans. Nucl. Sci.* **42** 2190 (1995)
123. Martin T, Koch A *J. Synchrotron Rad.* **13** 180 (2006)
124. Rack A et al. *Nucl. Instrum. Meth. Phys. Res. A* **586** 327 (2008)
125. Danilewsky A N et al. *Nucl. Instrum. Meth. Phys. Res. B* **266** 2035 (2008)
126. Kazimirov A et al. *J. Synchrotron Rad.* **13** 204 (2006)
127. Rack A et al. *J. Synchrotron Rad.* **17** 496 (2010)
128. Kohn V G, Argunova T S, Je J H *Appl. Phys. Lett.* **91** 171901 (2007)
129. Afanas'ev A, Kohn V *Kristallografiya* **22** 622 (1977)
130. Matsushita T, Hashizume H *Handbook of Synchrotron Radiation* (Amsterdam: North-Holland, 1983)
131. Dudley M, Huang X R, Huang W *J. Phys. D* **32** A139 (1999)
132. Vetter W, Dudley M *J. Appl. Cryst.* **34** 20 (2001)
133. Bowen D K, Tanner B K *High Resolution X-ray Diffractometry and Topography* (London: Taylor and Francis, 1998); Translated into Russian: *Vysokorazreshayushchaya Rentgenovskaya Difraktometriya i Topografiya* (St. Petersburg: Nauka, 2002)
134. Gutkin M Yu et al. *Appl. Phys. Lett.* **93** 151905 (2008)
135. Argunova T S, Kohn V G, Je J H *J. Surf. Investig.* **2** 861 (2008); *Poverkhnost* (12) 48 (2008)
136. Argunova T S et al. *Phys. Status Solidi A* **206** 1833 (2009)
137. Vodakov Yu A et al. *Phys. Status Solidi B* **202** 177 (1997)
138. ImageJ. Download, http://imagej.nih.gov/ij/download.html
139. Srolovitz D J et al. *Scripta Mater.* **39** 379 (1998)
140. Hirth J P *Acta Mater.* **47** 1 (1998)
141. Argunova T S et al., in *Physics and Technology of Silicon Carbide Devices* (Ed. Y Hijikata) (Croatia: Intech Publ., 2013) p. 27
142. Argunova T S et al. *Phys. Solid State* **57** 752 (2015); *Fiz. Tverd. Tela* **57** 733 (2015)
143. Ohsato H, Kato T, Okuda T *Mater. Sci. Semicond. Process.* **4** 483 (2001)
144. Ma X, Parker M, Sudarshan T S *Appl. Phys. Lett.* **80** 3298 (2002)
145. Strunk H P *J. Cryst. Growth* **160** 184 (1996)
146. Kamata I et al. *Jpn. J. Appl. Phys.* **39** 6496 (2000)
147. Epelbaum B M, Hofmann D J *J. Cryst. Growth* **225** 1 (2001)
148. Yakimova R et al. *J. Appl. Phys.* **98** 034905 (2005)
149. Gutkin M Yu et al. *J. Appl. Phys.* **92** 889 (2002)
150. Gutkin M Yu et al. *Phys. Status Solidi A* **209** 1432 (2012)
151. Sheinerman A et al. *Mater. Sci. Forum* **740 – 742** 597 (2013)
152. Kohn V G, Argunova T S, Je J H *J. Phys. D* **43** 442002 (2010)
153. Kohn V G, Argunova T S, Je J H *J. Surf. Invest.* **5** 1 (2011); *Poverkhnost* (1) 5 (2011)
154. Kohn V G, Argunova T S, Je J H *J. Surf. Invest.* **6** 840 (2012); *Poverkhnost* (10) 60 (2012)
155. Kohn V G, Argunova T S, Je J H *AIP Adv.* **3** 122109 (2013)
156. Kohn V G, Argunova T S, Je J H *AIP Adv.* **4** 097134 (2014)
157. Argunova T S et al. *Crystallogr. Rep.* **61** 914 (2016); *Kristallografiya* **61** 879 (2016)
158. Van Loan C *Computational Frameworks for the Fast Fourier Transform* (Philadelphia: SIAM, 1992)
159. Mancini L et al. *Phil. Mag. A* **78** 1175 (1998)
160. Gastaldi J et al. *J. Phys. D* **32** A152 (1999)
161. Agliozzo S et al. *Phys. Rev. B* **69** 144204 (2004)
162. Hwu Y et al. *J. Phys. D* **35** R105 (2002)
163. Baik S et al. *Rev. Sci. Instrum.* **75** 4355 (2004)
164. Hwu Y et al. *Phys. Med. Biol.* **49** 501 (2004)
165. Meuli R et al. *Eur. Radiol.* **14** 1550 (2004)
166. Tsai W L et al. *Nature* **417** 139 (2002)